

# HOLISMOKES XVI: Lens search in HSC-PDR3 with a neural network committee and post-processing for false-positive removal

S. Schuldt<sup>1,2</sup>, R. Cañameras<sup>3</sup>, Y. Shu<sup>4</sup>, I. T. Andika<sup>5,6</sup>, S. Bag<sup>5,6</sup>, C. Grillo<sup>1,2</sup>, A. Melo<sup>6,5</sup>,  
S. H. Suyu<sup>5,6</sup>, and S. Taubenberger<sup>5,6</sup>

<sup>1</sup> Dipartimento di Fisica, Università degli Studi di Milano, via Celoria 16, I-20133 Milano, Italy  
e-mail: stefan.schuldt@unimi.it

<sup>2</sup> INAF – IASF Milano, via A. Corti 12, I-20133 Milano, Italy

<sup>3</sup> Aix-Marseille Université, CNRS, CNES, LAM, Marseille, France

<sup>4</sup> Purple Mountain Observatory, No. 10 Yuanhua Road, Nanjing, Jiangsu, 210033, People’s Republic of China

<sup>5</sup> Technical University of Munich, TUM School of Natural Sciences, Physics Department, James-Franck-Straße 1, 85748 Garching, Germany

<sup>6</sup> Max-Planck-Institut für Astrophysik, Karl-Schwarzschild Straße 1, 85748 Garching, Germany

Received –; accepted –

## ABSTRACT

We have carried out a systematic search for galaxy-scale lenses exploiting multi-band imaging data from the third public data release of the Hyper Suprime-Cam (HSC) survey with the focus on false-positive removal, after applying deep learning classifiers to all ~110 million sources with  $i$ -Kron radius above  $0''.8$ . To improve the performance, we tested the combination of multiple networks from our previous lens search projects and found the best performance by averaging the scores from five of our networks. Although this ensemble network leads already to a false-positive rate (FPR) of ~0.01% at a true-positive rate (TPR) of 75% on known real lenses, we have elaborated techniques to further clean the network candidate list before visual inspection. In detail, we tested the rejection using SExtractor and the modeling network from HOLISMOKES IX, which resulted together in a candidate rejection of 29% without lowering the TPR. After the initial visual inspection stage to remove obvious non-lenses, 3,408 lens candidates of the ~110 million parent sample remained. We carried out a comprehensive multi-stage visual inspection involving eight individuals and identified finally 95 grade A (average grade  $G \geq 2.5$ ) and 503 grade B ( $2.5 > G \geq 1.5$ ) lens candidates, including 92 discoveries showing clear lensing features that are reported for the first time. This inspection also incorporated a novel environmental characterization using histograms of photometric redshifts. We publicly release the average grades, mass model predictions, and environment characterization of all visually inspected candidates, while including references for previously discovered systems, which makes this catalog one of the largest compilation of known lenses. The results demonstrate that (1) the combination of multiple networks enhances the selection performance and (2) both automated masking tools as well as modeling networks, which can be easily applied to hundreds of thousands of network candidates expected in the near future of wide-field imaging surveys, help reduce the number of false positives that is the main limitation in lens search to date.

**Key words.** gravitational lensing: strong – methods: data analysis – catalogs

## 1. Introduction

Strong gravitational lensing emerged in the past decades as a powerful tool to probe galaxy evolution and cosmology. It allows us to obtain in a very precise way the total mass (i.e., baryonic and dark matter) of the galaxy or galaxy cluster acting as the lens (e.g., Bolton et al. 2008; Shu et al. 2017; Caminha et al. 2019) and, by assuming that mass follows light, we can disentangle the mass components and obtain unique insights into the dark matter (DM) distribution (e.g., Schuldt et al. 2019; Shajib et al. 2021; Wang et al. 2022) or DM substructure (e.g., Enzi et al. 2024; Ertl et al. 2024; Lange et al. 2024). Thanks to the lensing magnification, strong lensing also allows us to study high-redshift sources not visible otherwise (e.g., Shu et al. 2018; Vanzella et al. 2021; Meštrić et al. 2022; Stiavelli et al. 2023; Morishita et al. 2024).

In case of a time variable background object, such as a supernova (SN) or a quasar, time delays can be measured (e.g., Courbin et al. 2018; Millon et al. 2020) and exploited for competitive measurements of the value of the Hubble constant  $H_0$  (Refsdal 1964). Given the rarity of SNe and strong lens-

ing events, this time-delay cosmography (TDC) technique was mostly carried out with quasars (e.g., Wong et al. 2020; Acebron et al. 2022; Shajib et al. 2022; Acebron et al. 2024). To date only three strongly lensed SNe are known with time delays usable for a precise measurement of  $H_0$ : SN Refsdal lensed by the cluster MACS J1149.5–2223 (e.g., Grillo et al. 2018; Kelly et al. 2023; Grillo et al. 2024), SN H0pe strongly lensed by the cluster PLCK G165.7+67.0 (Pascale et al. 2025), and SN Encore with SN Requiem both lensed by the same cluster MACS J0138–2155 (Ertl et al. in prep., Suyu et al. in prep., Pierel et al. in prep). To prepare a systematic search with the current and upcoming wide-field imaging surveys, we initiated the Highly Optimized Lensing Investigations of Supernovae, Microlensing Objects, and Kinematics of Ellipticals and Spirals (HOLISMOKES Suyu et al. 2020) program. As a precursor for the Legacy Survey of Space and Time (LSST) of the Vera C. Rubin Observatory (Ivezic et al. 2008; Ivezić et al. 2019), we are currently exploiting data from the Hyper Suprime-Cam (HSC), which are expected to be very similar.

In Cañameras et al. (2021, hereafter C21) we presented a residual neural network to search broadly for any static lens, and complemented this in Shu et al. (2022, hereafter S22) with lenses/deflectors at relatively high redshift ( $z_d \geq 0.6$ ) to better cover the whole redshift range. Both projects relied on a single convolutional neural network (CNN) and targeted HSC images of the second public data release (PDR2). In this work, we combine multiple networks into an ensemble network, relax our restrictions on filter coverage to increase the observed sky area (requesting *gri* bands instead of *grizy*), and consider data from PDR3 with slightly deeper and larger footprint.

While the resulting sample of network candidates from HSC is small enough for visual inspection, this will not be the case for LSST, *Euclid* (Laureijs et al. 2011), *Roman* (Spergel et al. 2015) and the Chinese Space Station Telescope (Gong et al. 2019), delivering more than a billion images, even with a citizen science approach (e.g., Holloway et al. 2024, Holloway et al in prep., Walmsley et al. in prep.). Consequently, we urgently need further automated ways to lower the false-positive rate (FPR) before an unavoidable visual inspection.

In this paper, we show our deep learning ensemble network and, following C21, apply it to cutouts of any object with *i*-Kron radius above  $0''.8$  that pass standardised HSC image quality flags (see C21 for details). We explore two different approaches to reject false positives: (1) we run SExtractor to reject images with artefacts or without a real astrophysical source in the cutout, followed by an exclusion through HSC-pixel flags, and (2), we run the residual neural network from Schuldt et al. (2023a, hereafter S23a) to reject systems based on the mass model predictions. Specifically, Sect. 2 presents the tested network committee and their performances on known real lenses. We then describe the two approaches of contaminant rejection in Sect. 3, before we carry out a visual inspection as described in Sect. 4 and present the newly discovered lens candidates. Finally, we give a summary and conclusion in Sect. 5. We exploit trained networks from C21, S22, and Cañameras et al. (2024, hereafter C24), and adopt consequently also a flat  $\Lambda$ CDM cosmology with  $\Omega_m = 1 - \Omega_\Lambda = 0.32$  (Planck Collaboration et al. 2020) and  $H_0 = 72 \text{ km s}^{-1} \text{ Mpc}^{-1}$  (Bonvin et al. 2017).

## 2. Inference with network committees

We followed the approach described in C21 to classify the  $\sim 110$  million galaxies from HSC Wide PDR3 with *i*-band Kron radius  $\geq 0''.8$  and optimize the contamination rate of the candidate strong lens sample. Based on test sets drawn from HSC Wide PDR2 images and designed to closely match a real classification setup, Cañameras et al. (2024) show that the purity and overall classification performance are significantly improved with committees of multiple neural networks (see also e.g., Andika et al. 2023). The highest gain is obtained when combining networks trained on different ground-truth data sets, with different prescriptions for the parameters' distributions over the mock lenses used as positive examples. Taking the average or multiplication of output scores from networks having little overlap in false positives due to their internal representations is best for improving the true-positive rate (TPR) at low FPR.

We investigated several combinations of neural networks chosen among the best performing ResNet and classical CNNs from C21, S22, and C24. After classifying the  $\sim 110$  million HSC PDR3 image cutouts with these networks, we compared the TPR over three independent sets of confirmed and candidate strong lenses as a function of the total number of lens candidates predicted by the committee. This allowed us to find the optimal

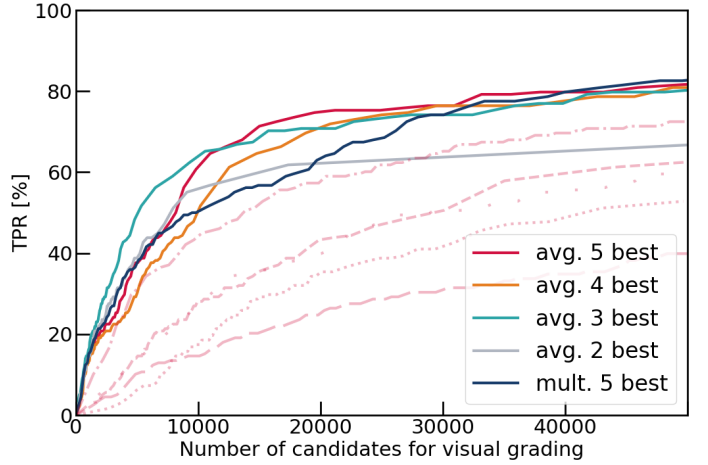


Fig. 1: True-positive rate (TPR) of different network committees (solid lines) against their predicted network candidate numbers measured on test set 3. We consider here five different networks, whose individual curves are shown in light-purple of various line styles. As examples, we show the performance of the ResNet trained on sets L4 and N1 from C24 (dash-dotted) and Classifier-1 from S22 (long-dotted). Gray solid line is the performance when averaging the scores from these two networks, green when additionally including the ResNet trained on L7 and N1 (long dashed), orange when also including the baseline ResNet from C24 (dotted), and red when additionally using the network from C21 (dashed). We further show the TPR evolution with a dark blue solid line when multiplying the network scores from all five networks instead of averaging.

committee that maximizes the TPR at a given output sample size (i.e. corresponding to a fixed human inspection time). The first set of test lenses (set 1) includes the 1,249 galaxy-scale grade A or B candidates from the SuGOHI papers\*. The second set (set 2) focuses on 201 galaxy-scale grade A from SuGOHI, which are also included in set 1. The third set (set 3) corresponds to the cleaned set of 178 galaxy-scale grade A or B lens candidates used in C21 C24, which excludes visually identified systems with multiple lens galaxies, or significant perturbation from the environment.

We investigated various combinations of different networks by taking the average or the product of their individual network scores. As examples, the performance of combinations with two, three, four, and five networks are shown in Fig. 1. The best committee that maximizes the TPR in all three test sets at fixed number of candidates was obtained by averaging the scores of five individual networks: the ResNet from C21, Classifier-1 from S22, and three additional ResNets from C24, as illustrated in Fig. 2. We adopted a threshold on the average score of 0.55, which corresponds to 22,393 strong-lens candidates, and a TPR of 51%, 54%, and 75% over test set 1, 2, and 3, respectively. Since the TPR curves reach a plateau for all of the three considered test sets, decreasing the score threshold to include 50,000 additional candidates would have improved the TPR by only  $\approx 4$ –5%, which does not justify the substantial increase in human inspection time. Having various test sets was important to check that the plateau in TPR is reached irrespective of the exact set-up of the test set. Since set 3 is representing best the galaxy-galaxy scale lenses we target with this network committee (e.g., set 3

\*see <https://www-utap.phys.s.u-tokyo.ac.jp/oguri/sugohi/>

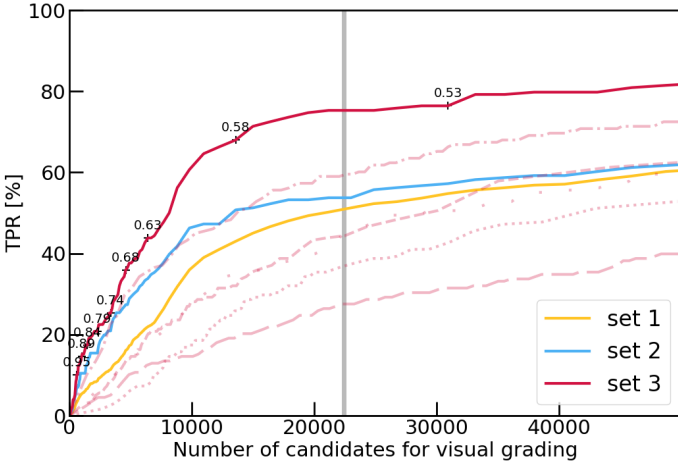


Fig. 2: Evolution of the true-positive rate (TPR), as measured over the three test sets of candidate and confirmed strong-lenses, as a function of the number of candidates selected by the neural networks. Solid curves show the results for the final committee of five networks trained on different ground-truth data sets. Light-purple curves show the lower TPR obtained on set 3 for the five individual networks included in the committee: the ResNet from C21 (dashed curve), Classifier-1 from S22 (long-dotted curve), the baseline ResNet from C24 (dotted curve), a network trained on mocks with natural  $\theta_E$  distribution (dash-dotted curve), and a ResNet trained on balanced fraction of doubles and quads (long-dashed curve). The vertical gray line marks the final score threshold applied to select the list of strong-lens network candidates. Examples of score thresholds are marked for the evaluation of the best committee on set 3.

is cleaned from group and cluster lenses), the network committee shows the best performance on this set as expected. Finding about 20,000 candidates among 110 million sources from the parent sample is consistent with the FPR in the range 0.01–0.03% predicted in C24 for networks committees, at a TPR of 75% evaluated among set 3.

The five networks are all from the same type of architecture and include residual neural network blocks (He et al. 2015). Specifically, the Classifier-1 from S22 is based on the CMU DeepLens package from Lanusse et al. (2018), while the other four networks are adapted from the ResNet-18 architecture. The networks were however trained on different ground-truth data sets. We introduce the general properties of the training sets and refer the reader to C21, S22, and C24 for further details.

For all five networks, the realistic mock lenses used as positive examples were simulated with the pipeline described in Schuldt et al. (2021, 2023b). Briefly, the pipeline paints lensed arcs on HSC images of massive luminous red galaxies (LRGs) using Singular Isothermal Ellipsoid (SIE) lens mass profiles, and SIE parameter values inferred from SDSS spectroscopic redshifts and velocity-dispersion measurements. After the high-redshift background sources are drawn from the *Hubble* Ultra-Deep Field (HUDF, Inami et al. 2017), mock lensed arcs are computed with GLEE (Suyu & Halkola 2010; Suyu et al. 2012b), and convolved with the HSC point spread function, before coaddition with the lens galaxy cutout. Positive examples used to train the ResNet from C21 and Classifier-1 from S22 were drawn from the same parent set of mocks, with (i) nearly-uniform Einstein radius distribution between  $0''.75$  and  $2''.5$ , (ii) a boosted fraction of lens galaxies at  $z > 0.7$  with respect to the parent

Table 1: Summary of the different selection stages with corresponding sample size, including re-discoveries.

Description	Sample size	Section
Parent sample (in million)	~110	2
Network candidates	22,393	2
After SExtractor cleaning	19,820	3.1
After pixel level cuts	18,712	3.1
After CNN lens model cleaning	15,919	3.2
After excluding duplicates ( $< 2''$ )	14,448	4
After excluding previous inspected systems	11,773	4
Inspected in binary classification round	11,874	4.1
Inspected by first team	3,408	4.2
Recentered after first team’s inspection	160	4.2
Inspected by second team	686	4.2
Total inspected systems listed in Table 2	14,152	4.4
New published grade A (B) lens candidates	9 (83)	4.4
New inspected grade A (B) lens candidates	42 (187)	4.4
All grade A (B) lens candidates	95 (503)	4.4
Grade A (B) lens candidates with $OD_{vis}$	22 (66)	4.5
Grade A (B) lens candidates with $OD_z$	18 (70)	4.5
New inspected grade A with good model	28 (67%)	4.5
New inspected grade B with good model	164 (88%)	4.5
Inspected grade A or B with good model	192 (84%)	4.5

SDSS sample, (iii) lensed images having  $\mu \geq 5$ , and (iv) a minimal ratio  $SNR_{bg,min} = 5$  between the brightest arc pixel and the local sky background over the lens LRG cutout. The other three high-performing networks from C24 that are part of the committee were trained on mocks produced with a similar procedure, but with (i) a boosted fraction of red HUDF sources, (ii) a natural Einstein radius distribution between  $0''.75$  and  $2''.5$  instead of uniform distribution, and (iii) no lower limit on  $\mu$  and a balanced fraction of double and quad configurations. This corresponds to sets labeled L1, L4, and L6 in C24.

In terms of negative examples, four out of the five networks include a mix of 33% spirals, 27% isolated LRGs without arcs, 6% groups, and 33% random galaxies over the HSC footprint, as defined for set N1 in C24. The fifth network, namely Classifier-1 from S22, was primarily targeting high-redshift strong-lenses and trained on negative examples drawn from a parent sample with red ( $g-r$ ) and ( $g-i$ ) colors. All five networks were trained and validated on images in *gri* bands, such that we require only the availability of *gri* bands in HSC while the image in *z* or *y* can be missing.

### 3. Cleaning the output candidate list

Before conducting a visual inspection (see Sect. 4) to identify the high-quality strong lens candidates, the catalog of 22,393 candidates was post-processed to remove obvious artefacts and non-lenses. Here we applied mainly two criteria, as detailed below. An overview table of the stages and resulting sample sizes is given in Table 1.

#### 3.1. Cleaning using SExtractor and HSC pixel level flags

A substantial fraction of contaminants correspond to cutouts with residual background emission in one or all *gri* bands (see some examples in the top row of Fig. 3). These cutouts were identified using source masking and estimates of the sky background with SExtractor (Bertin & Arnouts 1996), leaving 19,820

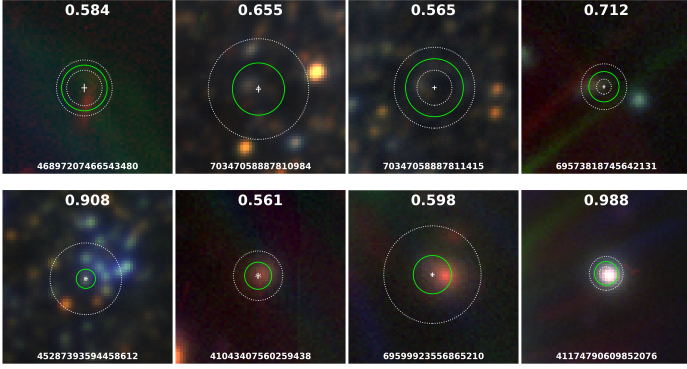


Fig. 3: Examples of false-positive candidates from the network committee that were cleaned with post-processing scripts. A major fraction of contaminants correspond to crowded fields and/or cutouts with non-zero background emission in  $g$ ,  $r$ , and/or  $i$ -band, which are rejected by SExtractor and HSC pixel-level flags (top row) or by the modeling network from S23a (bottom row). We show the average score of the network committee and the HSC ID in the top and bottom, respectively, of each panel, which is  $\sim 10''$  on a side. We further show the predicted lens center as cross with length corresponding to the predicted uncertainty, and the Einstein radius as green solid circle with predicted uncertainty bounds as white dotted lines. Some of the lower limits on the Einstein radii are near zero and are thus not visible.

candidates without loss of any test lens. This step was then refined with information from the pixel-level flags inferred by the HSC pipeline. We searched for optimal cuts to remove contaminants using the flags in  $gri$  bands over the  $72 \times 72$  pixel images. First, we discarded cutouts having  $>90\%$  pixels with flags  $\geq 512$  and  $<1024$ , corresponding to pixels located near a bright object. This securely excluded cutouts affected by bright neighboring stars within a few tens of arcseconds. Secondly, we removed cutouts with  $>99\%$  pixels flagged as “detected pixels”, which are more likely to correspond to crowded fields such as stellar clusters, or star-forming clumps within extended disks, than strong gravitational lenses. These two criteria decreased the sample to 18,712 candidates.

### 3.2. Cleaning using modeling CNN

In parallel, we applied the ResNet from S23a to all 22,393 network candidates. This modeling network is trained on realistic mock images created in a similar way as those used for training the committee network, and obtained great performance in measuring the Einstein radii of lens systems when compared to *glee\_auto.py* (Schuldt et al. 2023b), a code that relies on the well-tested lens modeling software GLEE (Suyu & Halkola 2010; Suyu et al. 2012a). The modeling network predicts the lens mass center  $x$  and  $y$ , the lens mass ellipticity  $e_x$  and  $e_y$ , and Einstein radius  $\theta_E$  of a SIE profile as well as an external shear ( $\gamma_1$  and  $\gamma_2$ ), and the corresponding  $1\sigma$  uncertainties.

Since the modeling network is trained on solely lens images (i.e. not in combination with lens classification as in Andika et al. (2024)), it is forced to provide reasonable model parameters (e.g.,  $\theta_E \in [0'.5, 5'']$ ) even if the given image is clearly not a lens. However, for such a given non-lens image, the modeling network is uncertain and the predicted errors can be significantly higher. Consequently, we can use this fact to reject false-positives from the classification network. To be conservative, we

define the cuts here such that we do not exclude any lens candidate from our test set as shown in Fig. 4, which results in an additional rejection of 2,794 systems. We show some examples of rejected candidates in the bottom row of Fig. 3.

In sum, we reject around 29% of the network candidates as false positives by keeping the same TPR on our test sample. This cleaning is performed through automated and fast scripts and thus are also scalable for sample sizes expected from ongoing and upcoming wide-field imaging surveys which are two orders of magnitude higher. While excluding  $\sim 1/3$  of the contaminants by keeping the same TPR is already a good improvement in the purity, we note that for significantly higher samples more stringent cuts can be applied to reject more contaminants with the downside of possibly excluding some lenses.

## 4. Visual inspection

Before the visual inspection of the remaining network candidates from Sect. 3, we excluded duplicates among the network candidates. Although CNNs are known to be translation invariant, we only excluded duplicates within two pixels when creating the 110 million parent sample to be very conservative. This ensures that we will not miss any candidate from the network due to a lower score if the lens is not well centered or partly out of the cutout. However, for the visual inspection, we removed duplicate cutouts within  $2''$ . In order to preserve lines of sight with the most extended, and most likely deflector galaxy in the center, we rank ordered the catalog entries by decreasing  $i$ -Kron radius and removed duplicates of lower rank. Excluding these duplicates reduces the human inspection time further, while the moderate cut of  $2''$  ensures that we will not shift any multiple image out of the inspected cutout that would risk missing the identification.

Furthermore, we excluded additional image stamps previously inspected as part of our HOLISMOKES strong lens searches in earlier HSC data releases (C21; S22; Schuldt et al. (2025), hereafter S25) to lower the need in human resources, as we grade the systems in a similar way and would therefore have similar resulting grades. We only kept 50 lenses (high-quality grade A or B lens candidates, which we simply refer to as “lenses” hereafter) and 50 non-lenses from C21 and S25 relying both on the same network, as well as 50 lenses and 50 non-lenses from S22 for comparison<sup>†</sup>. This resulted in a catalog of 11,874 candidates for visual inspection.

The visual inspection follows closely the procedure proposed by S25 and was conducted jointly with candidates presented by Andika et al. (2024). In short, we first carried out a calibration round using 200 system inspected by all eight inspectors<sup>‡</sup> since we introduced several new features in the grading tool as detailed below. As previously, we use a three-panel image to show two different scalings of the  $gri$  bands, and, in contrast to previous inspections, an image of the  $riz$  bands to ease the identification of lensed quasars. While these image stamps have a size of  $10'' \times 10''$ , we additionally show  $80'' \times 80''$  stamps in the same filters and scaling as in the smaller cutout.

<sup>†</sup>we use here a lower limit of the threshold score  $p = 0.53$  to include also a few systems that would be usually excluded with the cut at  $p = 0.55$ .

<sup>‡</sup>The visual inspectors are in alphabetical order by last name: I. T. A., S. B., R. C., C. G., A. M., S. S., S. H. S., and S. T.

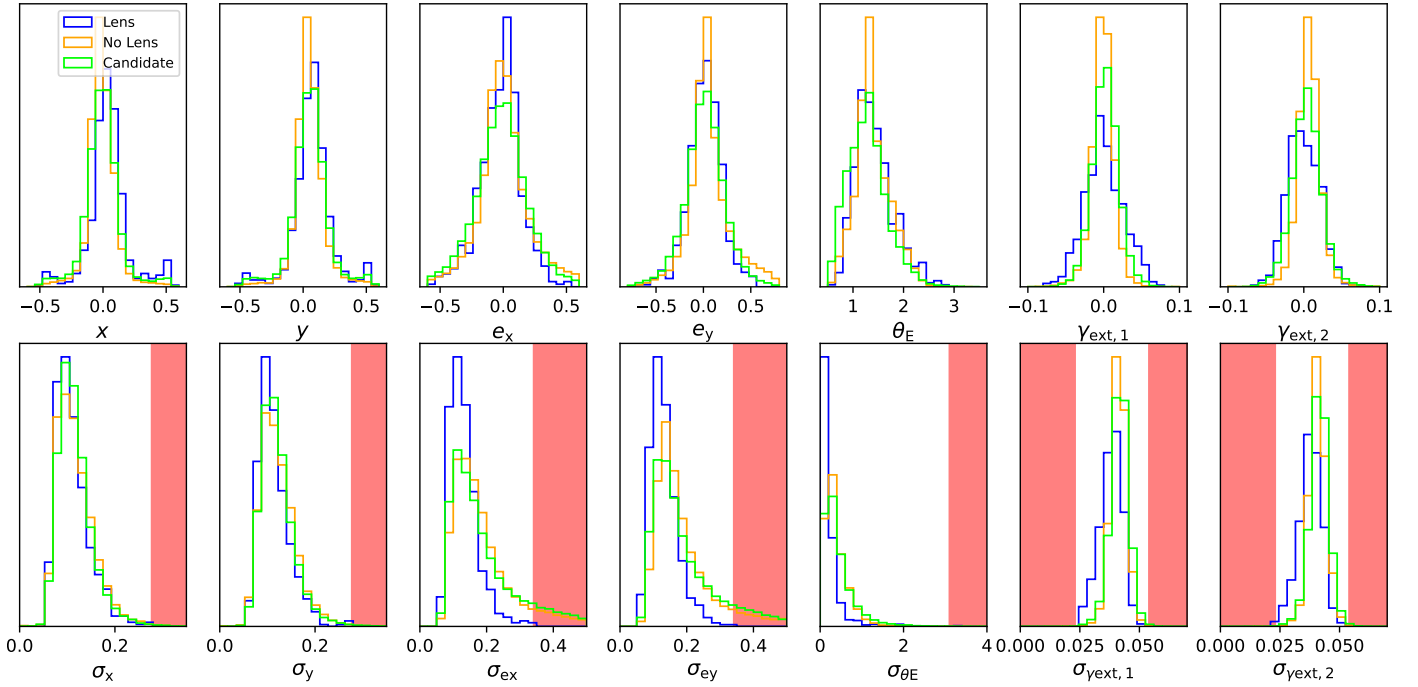


Fig. 4: Normalized histograms of the mass model parameter predictions using the modeling network from S23a. The top row shows the predicted mass model parameter values, and the bottom row shows the corresponding  $1\sigma$  uncertainties. We show the 546 grade A and B lens candidates from C21 and S25 (blue), the visually rejected systems as non-lenses for comparison (orange), and those of the network candidates from our committee network of this work (green). The parameter ranges used to reject non-lenses are marked in red and defined by the largest/lowest uncertainty of the above mentioned grade A and B lens sample (the small overlaps between the red regions and non-zero blue bins are merely due to the finite bin widths of the histograms).

#### 4.1. Binary inspection

We then split the catalog among ourselves, such that each system is inspected by two graders in a binary classification to exclude rapidly the majority of obvious non-lenses. As mentioned above, the catalog contains 200 systems from our previous searches, with 100 lenses and 100 non-lenses. Of the 100 lenses (or lens candidates), we recovered 98/100 with previous grade A or B and only missed two systems, namely, systems HSC J222002+060506<sup>§</sup> and HSC J090929+010030 which previously obtained both an average grade of 1.6 while the lower limit for grade B is 1.5. Of the 100 non-lenses, we forwarded 59/100, which, however, is understandable as several of these galaxies obtained previously an average grade slightly below 1.5 and we aimed on forwarded now all systems above a grade of 1 in the final grading scheme. Interestingly, we also forwarded 12/100 with previously average grade 0. Since this first stage is graded conservatively to rule out obvious non-lenses and there is subsequently another round of inspection for refinement, this result on the 200 systems is overall very good.

#### 4.2. Multi-class inspection

In the next round, four individuals inspected the remaining 3,408 systems from the binary classification. At this stage, each inspector provided one of four possible grades (0 corresponding to “no lens”, 1 to “possible lens”, 2 to “probable lens”, and 3 to “definite lens”) and voted in case the lens is significantly offset from the cutout center. In total, 309 systems obtained the “off-center” flag by at least one person, such that the lens center was

subsequently corrected. A re-centering at this stage was crucial for the subsequent round of grading by the other four remaining graders, as we also showed in the central image the lens center and Einstein radius predicted by the ResNet from S23a (see bottom row of Fig. 3 for examples).

Based on the average grade  $G$  obtained from these four grades, we forwarded all systems with either  $G > 1$  or  $G \leq 1$  but standard deviation of the four grades above 0.75. Including those with lower grade but high discrepancy increases the forwarded sample significantly, but minimises the possibility of missing any good lens candidate. This resulted in 686 candidates, including 160 systems that got shifted, which were inspected by the remaining four graders. In addition to the grading and “off-center” flag from the previous round, these four individuals were tasked to also indicate if the predicted lens center or Einstein radius is significantly mis-predicted. Furthermore, for each candidate, two histograms of photometric redshifts from the lens candidate environment, one up to  $z = 1$  and the other up to  $z = 4$ , were shown in order to obtain a classification of the environment as well. As examples, the histograms of one system in an overdensity (bottom row) and one in the field (top row), are shown in Fig. 5. This allows us to assess if the predicted mass model, which we provide in Table 2 (see also Table 3 for explanations), is reliable and to characterise their environment, while increasing the visual inspection time only very little.

#### 4.3. Comparison to previous inspected candidates

As mentioned above, we included 200 systems that we inspected already in previous works. From the 100 candidates that we previously excluded (i.e. that obtained an average grade  $G < 1.5$ ),

<sup>§</sup>Listed as HSC J2220+0605 in C21.

Table 2: Lens candidates with network committee scores  $p \geq 0.55$  that are visually inspected (excluding duplicates). The full table is available in electronic form and each column content explained in Table 3.

Name (1)	RA [deg] (2)	Dec [deg] (3)	$p$ (4)	$G$ (5)	$\sigma_G$ (6)	$N_{\text{graders}}$ (7)	$\theta_E$ ["] (24)	$\sigma_{\theta_E}$ (25)	Model (30)	$z$ (31)	References (37)
HSCJ1004-0031	151.21543	-0.52911	0.64	3.00	0.00	8	1.44	0.15	Y	1.05	A23
HSCJ2305-0002	346.34026	-0.03658	0.60	3.00	0.00	8	1.32	0.12	Y	0.49	W18 C21
HSCJ2242+0011	340.58995	0.19573	0.71	3.00	0.00	8	1.51	0.11	Y	0.38	S18 R22
HSCJ1236-0035	189.15056	-0.59418	0.86	3.00	0.00	8	0.90	0.06	Y	0.49	S22
HSCJ0102+0159	15.65957	1.98211	0.61	3.00	0.00	8	1.38	0.09	N	0.95	J19 C21
⋮	⋮	⋮	⋮	⋮	⋮	⋮	⋮	⋮	⋮	⋮	⋮

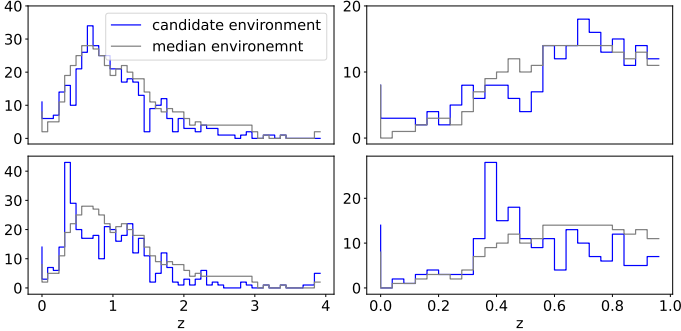


Fig. 5: Histograms of the photometric redshifts within a box of  $200''$  on a side around two different lens candidates (top/bottom row) as examples. Such histograms, one in the range up to a redshift of 4 (left) and one up to a redshift of 1 (right), were shown during the visual inspection to ease the environment classification. The lens system in the top row has an environment similar to the median, whereas the system in the bottom row shows an overdensity at  $z \sim 0.4$ .

only one system obtained now an average grade above 1.5 and is consequently listed as grade B candidate. From the sample of previously classified grade A and B lenses, we notice a tendency towards lower grades consistently among most graders. While there were some changes compared to previous inspections, such as moving from PDR2 to PDR3 and showing two *gri* color images and one *riz* color image instead of three *gri* color images, we ruled these aspects out by directly comparing some inspected images from S25 and this work. We note also that the applied scalings depend on the pixel values of the given cutout, such that a shifted image appears slightly different. Additionally, in S22 we focused on high- $z$  lenses and applied slightly different scaling functions, but find this to be not a major reason. Furthermore, we speculate that this tendency may come from the relatively pure sample (i.e., a higher proportion of lenses) that we had after the binary inspection, but note that we also had in previous works a binary inspection cleaning carried out by a single inspector, resulting in a comparably pure sample. In contrast, we noticed that the  $80'' \times 80''$  cutouts help in specific cases to reject non-lenses as the overall environment is visible. Finally, we remark that it is known (Rojas et al. 2023; Schuldt et al. 2025) that every grader has a different expectation and also the grades among a single inspector varies. Consequently, it might be simply that our expectations for an object to qualify as a lens candidate has slightly increased over time, possibly because of the increasing sample of lenses and the higher availability of high-resolution images

(e.g., Euclid, see Acevedo Barroso et al. (2024); Nagam et al. (2025), Walmsley et al. in prep.).

#### 4.4. Final lens compilation

Despite the tendency towards lower grades, we adopt our traditional cuts to define grade A ( $3 \geq G \geq 2.5$ ) and grade B ( $2.5 > G \geq 1.5$ ), and release in Table 2 the full catalog of visually inspected systems. This catalog includes jointly inspected systems that obtained a committee score  $p \geq 0.53$  and were also detected by VariLens (Andika et al. 2024, noted in column 12 of the catalog), but we exclude any duplicates within  $< 2''$ . Consequently, using the average grades  $G$  of all eight inspectors to obtain a stable average (see also Rojas et al. 2023; Schuldt et al. 2025), we found 42 grade A and 187 grade B lens candidates, which are listed in Table 2. Furthermore, the newly discovered grade A candidates are shown in Fig. 6, while the grade B systems are shown in Fig. 7. We further provide in this table all grade A and B lens candidates from C21 (marked in column 15, see Table 3), S22 (marked in column 14), and S25 (marked in column 13) which we detected with our network committee as candidate but excluded for visual inspection (see also Sect. 4.2). In sum, we found with our network committee 95 grade A and 503 grade B lenses. From these systems, 506 systems (included not re-graded systems) were already known, while we show in Figs. A.1 (grade A) and A.2 (grade B) those that we re-graded in our inspection (either because they are in the small comparison sample, see Sect. 4.3, or because they were discovered by other work and not by C21, S22, or S25). This high recovery rate is expected, given the enormous lens search projects that already exploited HSC data and in particular our previous searches using individual networks that entered into our network committee now. However, we remind the reader that the new lens identification is only one aspect of this work.

#### 4.5. Discussion on the lens properties

We further classified the lens environment using photo- $z$  histograms during the inspection by the second team (see Fig. 5 for examples), leading to an identification of 147 candidates in an overdensity (corresponding to at least two votes) of which 22 and 66 are ranked as grade A and B candidates, respectively. With the automated photo- $z$  procedure to identify overdensities presented by S25, we identify 569 systems among the whole inspected sample, of which 18 and 70 are classified as grade A or B lens candidates, respectively (see also Tab. 1). While the automated procedure can be easily applied to large samples, the visual classification requires in particular human time that is

Table 3: Detailed description of the released catalog, as previewed with five lines in Table 2 for a selected subset of columns.

Column	Header	Description
(1)	Name	name for grade A and B lens candidates
(2)	RA [deg]	Right Ascension in degrees of the inspected candidate
(3)	Dec [deg]	Declination in degrees of the inspected candidate
(4)	p	average score predicted by the network committee
(5)	G	average grade between 0 and 3 obtained through visual inspection (see Sect. 4)
(6)	sigma_G	standard deviation of obtained visual inspection grades.
(7)	N_graders	number of visual inspectors (see Sect. 4)
(8)	$i$ _kronflux_radius	Kron radius in the $i$ band provided by HSC used for source selection (see Sect. 2)
(9)	Binary	Flag to indicate sources inspected only in the binary stage (two different graders)
(10)	Round1	Flag to indicate systems inspected also in the first round (four different graders)
(11)	Round2	Flag to indicate systems inspected also in the second round (eight different graders)
(12)	A24	Flag to indicate if system jointly inspected with candidates discovered by Andika et al. (2024)
(13)	S25	Flag to indicate systems discovered by this network committee but not re-inspected. Instead, we report the visual inspection grade from our earlier work S25
(14)	S22	Flag to indicate systems discovered by this network committee but not re-inspected. Instead, we report the visual inspection grade from our earlier work Shu et al. (2022)
(15)	C21	Flag to indicate systems discovered by this network committee but not re-inspected. Instead, we report the visual inspection grade from our earlier work Cañameras et al. (2021)
(16)	x_med	$x$ -center coordinate predicted by the modeling network from Schuldt et al. (2023a, hereafter S23a)
(17)	x_err	$1-\sigma$ value for the $x$ -center coordinate predicted by the modeling network from S23a
(18)	y_med	$y$ -center coordinate predicted by the modeling network from S23a
(19)	y_err	$1-\sigma$ value for the $y$ -center coordinate predicted by the modeling network from S23a
(20)	ex_med	$x$ -component of the complex ellipticity predicted by the modeling network from S23a
(21)	ex_err	$1-\sigma$ value for the $x$ -component of the complex ellipticity predicted by the modeling network from S23a
(22)	ey_med	$y$ -component of the complex ellipticity predicted by the modeling network from S23a
(23)	ey_err	$1-\sigma$ value for the $y$ -component of the complex ellipticity predicted by the modeling network from S23a
(24)	rE_med	Einstein radius value of the given candidate predicted by the modeling network from S23a
(25)	rE_err	$1-\sigma$ value of the Einstein radius predicted by the modeling network from S23a
(26)	gam1_med	$\gamma_1$ -component of the external shear predicted by the modeling network from S23a
(27)	gam1_err	$1-\sigma$ value of the $\gamma_1$ -component predicted by the modeling network from S23a
(28)	gam2_med	$\gamma_2$ -component of the external shear predicted by the modeling network from S23a
(29)	gam2_err	$1-\sigma$ value of the $\gamma_2$ -component predicted by the modeling network from S23a
(30)	Model	Flag if the model predict is reliable, only for systems inspected in the second round
(31)	z	photometric redshift value from the catalog compiled catalog by S25 based on DEmP (Hsieh & Yee 2014), Mizuki (Tanaka et al. 2018), and NetZ (Schuldt et al. 2021)
(32)	OD_vis	Flag if the system falls into a significant overdense region
(33)	OD_z	Flag if the system is in a significant overdense environment according to the criteria defined by S25
(34)	N_max	Peak of the photo- $z$ histogram following the procedure of S25
(35)	zlow	Lower bound of N_max in the photo- $z$ histogram indicating the redshift of the overdensity
(36)	Ntot	Sum of objects with photo- $z$ within a box of $200''$ on a side.
(37)	References	List of publications that report the inspected candidate (within $5''$ ) as lens candidate according to the HOLISMOKES Suyu et al. (2020) lens compilation with status of the publication, using B04 for Bolton et al. (2004), C07 for Cabanac et al. (2007), B08 for Bolton et al. (2008), G14 for Gavazzi et al. (2014), H15 for Holwerda et al. (2015), M16 for More et al. (2016), P16 for Paraficz et al. (2016), S16 for Shu et al. (2016), D17 for Diehl et al. (2017), J17 for Jacobs et al. (2017), S18 for Sonnenfeld et al. (2018), W18 for Wong et al. (2018), J19 for Jacobs et al. (2019), L19 for Li et al. (2019), P19 for Petrillo et al. (2019), H20 for Huang et al. (2020), C20 for Chan et al. (2020), Ca20 for Cañameras et al. (2020), Cao20 for Cao et al. (2020), L20 for Li et al. (2020), J20 for Jaelani et al. (2020), S20 for Sonnenfeld et al. (2020), C21 for Cañameras et al. (2021), H21 for Huang et al. (2021), L21 for Li et al. (2021), T21 for Talbot et al. (2021), R22 for Rojas et al. (2022), S22 for Shu et al. (2022), Sa22 for Savary et al. (2022), St22 Stein et al. (2022), W22 for Wong et al. (2022), Z22 for Zhong et al. (2022), A23 for Andika et al. (2023), J24 for Jaelani et al. (2024), G24 for Grespan et al. (2024), St24 for Storfer et al. (2024), S25 for Schuldt et al. (2025), ML for the master lens catalog at <a href="http://admin.masterlens.org">http://admin.masterlens.org</a> , and ‘Guoyou Sun’ corresponds to candidates identified by an amateur astronomer, Guoyou Sun, through visual inspections of HSC cutouts (see <a href="http://sunguoyou.lamost.org/glc.html">http://sunguoyou.lamost.org/glc.html</a> ).

highly limited. On the other hand, we visually identified several systems to be in an overdensity that are missed by the automated procedure due to missing  $z$  or  $y$  band observations required for the photo- $z$  codes. In total, we find a good overlap between the two complementary procedures.

As mentioned earlier, we further showed the network predicted lens center and Einstein radius during final inspection.

Since we found in the calibration round that the model network from Schuldt et al. (2023a) has difficulties to correctly predict the model if the lens is not well centered, we mitigated this through a re-centering between the last two inspection stages. We overlay the predicted lens center and Einstein radius on the cutouts of our lens candidates in Appendix B. For the reported lens center coordinates in Table 2, we only found 9% of the

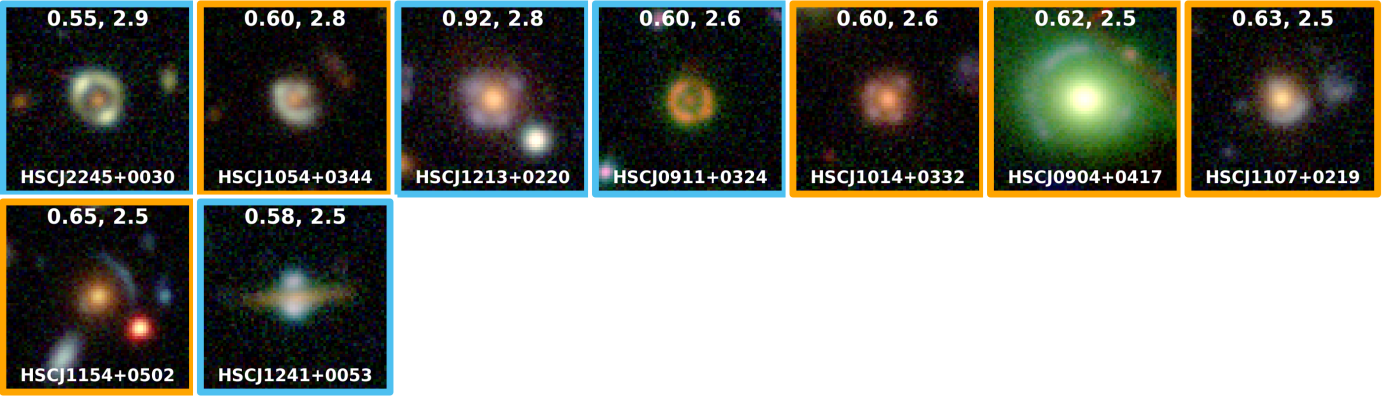


Fig. 6: Color-image stamps ( $12'' \times 12''$ ; north is up and east is left) of identified grade-A lens candidates using HSC PDR3 *gri* multi-band imaging data that are detected for the first time. At the top of each panel, we list the scores of the network committee,  $p$ , and the average visual inspection grade,  $G$ , of eight graders, where  $\geq 2.5$  corresponds to grade A. At the bottom, we list the candidate name. We further distinguish between candidates discovered jointly with Andika et al. (2024) using VariLens, appearing with blue frames, and fully new identifications with orange frames. All systems with their coordinates and further details such as the lens environment and Einstein radii are listed in Table 2.

lens candidates to have a relatively poor predicted lens center or Einstein radius which might be because of a group- or cluster-scale lens not suited for the modeling network or a remaining offset of the lens. We provide the predicted values of the seven mass model parameters with their corresponding  $1-\sigma$  uncertainties in Table 2 (columns 16 to 29, see also Table 3) as well as a flag (column 30) if the lens center and Einstein radius are matching reasonably the system (defined as two or more votes). This demonstrates once more the power of the modeling network and shows that the result can be used for further analysis.

While we applied in Sect. 3.2 relatively weak cuts on the model parameter uncertainties (see Fig. 4), we note that more stringent cuts are possible when the sample sizes are becoming significantly larger. This would lead to an even higher fraction of systems that can be easily ruled out, while keeping most of the lens candidates.

## 5. Summary and Conclusion

We have carried out a systematic search for strong gravitational lenses using the *gri* bands of the HSC Wide layer observations from the third public data release. For this, we tested the combination of different networks by averaging or multiplying their individual network scores. The best performance, 75% completeness on real lenses at a FPR of  $\sim 0.01\%$ , was obtained by averaging the scores from five different networks.

While the resulting sample size would have been easily possible to visually inspect, this will change with the next generation of wide-field imaging surveys, such that further cleaning is unavoidable. We tested two approaches, first using SExtractor and the HSC pixel-level flags to reject images with mostly non-zero background or image artefacts, and second, the ResNet modeling network from Schuldt et al. (2023a) as it predicts higher uncertainties for non-lenses. This lowered the contaminants by 29%, while not excluding any lens candidate from our previous identifications. Such post-processing scripts are expected to play a crucial role when two orders of magnitude more images need to be classified.

Thanks to a visual inspection of the cleaned network candidate list, we identified 95 grade A and 503 grade B candidates, which include 506 previously known systems. We provide in

Table 2 their coordinates together with their SIE and external shear parameters obtained from the ResNet presented by Schuldt et al. (2023a). During visual inspection, we also showed, which was done for the first time, the predicted lens center and Einstein radius and characterized the reliability. We found that only  $\sim 9\%$  of the candidates obtained a lens center or Einstein radius that is not well predicted, once the system is well centered. Moreover, we characterized their environment with two complementary approaches, either through visual inspection of histograms showing the photo- $z$  values of their surrounding, or the selection cuts elaborated by S25. In both cases, we find 88 grade A or B systems to be in a significant overdense environment. By releasing Table 2, which includes all visually inspected candidates with our obtained average grades and their characteristics as well as their previous discoveries, we release one of the most complete catalogs of strong lensing systems so far.

Particularly in preparation for the ongoing and upcoming wide-field imaging surveys, the removal of false-positives of network classifiers will be a challenge, such that the approaches presented here are expected to play a crucial role. Furthermore, fast and autonomous techniques to characterize and analyze the new systems, as tested here as well, will be the challenge we face.

## Data Availability

Table 2 will be available after acceptance of the publication at the CDS via anonymous ftp to [cdsarc.cds.unistra.fr](ftp://cdsarc.cds.unistra.fr) (130.79.128.5) or via <http://cdsweb.u-strasbg.fr/cgi-bin/qcat?J/A+A/>. It will be further released through the HOLISMOKES collaboration webpage at [www.holismokes.org](http://www.holismokes.org) and accordingly incorporated in the SuGOHI data base accessible through <https://www-utap.phys.s.u-tokyo.ac.jp/~oguri/sugohi/>.

*Acknowledgements.* SS has received funding from the European Union's Horizon 2022 research and innovation programme under the Marie Skłodowska-Curie grant agreement No 101105167 — FASTIDIoUS. We acknowledge financial support through grants PRIN-MIUR 2017WSCC32 and 2020SKSTHZ. This project has received funding from the European Research Council (ERC) under the European Union's Horizon 2020 research and innovation programme (LENSNOVA: grant agreement No 771776). This research is supported in part by the Excellence Cluster ORIGINS which is funded by the





Fig. 7: Color-image stamps of newly identified grade-B lens candidates. Same format as Fig. 6

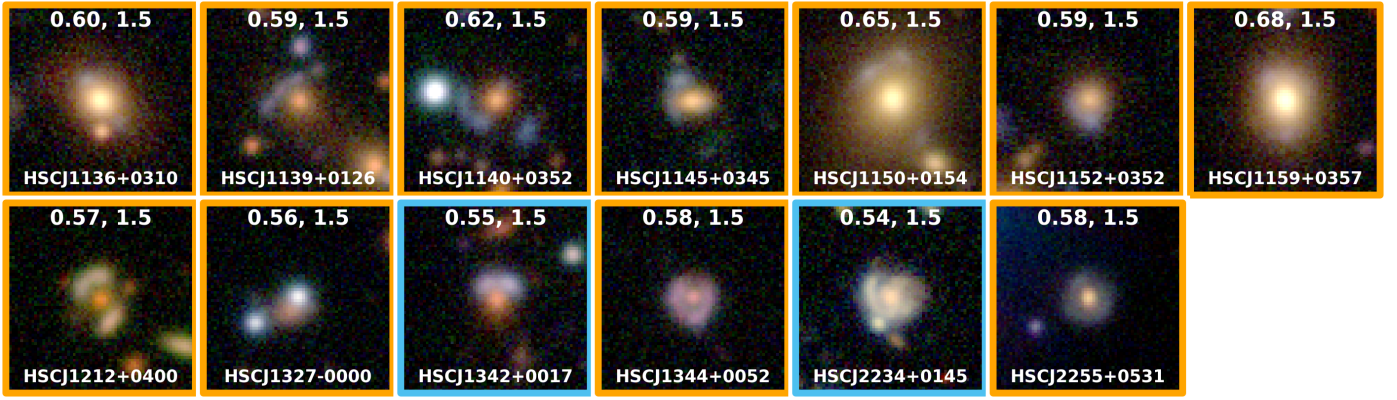


Fig. 7 (continued): Color-image stamps of newly identified grade-B lens candidates. Same format as Fig. 6

Deutsche Forschungsgemeinschaft (DFG, German Research Foundation) under Germany's Excellence Strategy – EXC-2094 – 390783311. This work uses the following software packages: *Astropy* (Astropy Collaboration et al. 2013; Price-Whelan et al. 2018), *matplotlib* (Hunter 2007), *NumPy* (van der Walt et al. 2011; Harris et al. 2020), *Python* (Van Rossum & Drake 2009), *Scipy* (Virtanen et al. 2020).

## References

- Acebron, A., Grillo, C., Bergamini, P., et al. 2022, *A&A*, 668, A142  
 Acebron, A., Grillo, C., Suyu, S. H., et al. 2024, *ApJ*, 976, 110  
 Acevedo Barroso, J. A., O’Riordan, C. M., Clément, B., et al. 2024, arXiv e-prints, arXiv:2408.06217  
 Andika, I. T., Schuldt, S., Suyu, S. H., et al. 2024, arXiv e-prints, arXiv:2412.12709  
 Andika, I. T., Suyu, S. H., Cañameras, R., et al. 2023, *A&A*, 678, A103  
 Astropy Collaboration, Robitaille, T. P., Tollerud, E. J., et al. 2013, *A&A*, 558, A33  
 Bertin, E. & Arnouts, S. 1996, *A&AS*, 117, 393  
 Bolton, A. S., Burles, S., Schlegel, D. J., Eisenstein, D. J., & Brinkmann, J. 2004, *AJ*, 127, 1860  
 Bolton, A. S., Treu, T., Koopmans, L. V. E., et al. 2008, *ApJ*, 684, 248  
 Bonvin, V., Courbin, F., Suyu, S. H., et al. 2017, *MNRAS*, 465, 4914  
 Cañameras, R., Schuldt, S., Shu, Y., et al. 2024, *A&A*, 692, A72  
 Cañameras, R., Schuldt, S., Shu, Y., et al. 2021, *A&A*, 653, L6  
 Cañameras, R., Schuldt, S., Suyu, S. H., et al. 2020, *A&A*, 644, A163  
 Cabanac, R. A., Alard, C., Dantel-Fort, M., et al. 2007, *A&A*, 461, 813  
 Caminha, G. B., Rosati, P., Grillo, C., et al. 2019, *A&A*, 632, A36  
 Cao, X., Li, R., Shu, Y., et al. 2020, *MNRAS*, 499, 3610  
 Chan, J. H. H., Suyu, S. H., Sonnenfeld, A., et al. 2020, *A&A*, 636, A87  
 Courbin, F., Bonvin, V., Buckley-Geer, E., et al. 2018, *A&A*, 609, A71  
 Diehl, H. T., Buckley-Geer, E. J., Lindgren, K. A., et al. 2017, *ApJS*, 232, 15  
 Enzi, W. J. R., Krawczyk, C. M., Ballard, D. J., & Collett, T. E. 2024, arXiv e-prints, arXiv:2411.08565  
 Ertl, S., Schuldt, S., Suyu, S. H., et al. 2024, *A&A*, 685, A15  
 Gavazzi, R., Marshall, P. J., Treu, T., & Sonnenfeld, A. 2014, *ApJ*, 785, 144  
 Gong, Y., Liu, X., Cao, Y., et al. 2019, *ApJ*, 883, 203  
 Grespan, M., Thuruthipilly, H., Pollo, A., et al. 2024, *A&A*, 688, A34  
 Grillo, C., Pagano, L., Rosati, P., & Suyu, S. H. 2024, *A&A*, 684, L23  
 Grillo, C., Rosati, P., Suyu, S. H., et al. 2018, *ApJ*, 860, 94  
 Harris, C. R., Millman, K. J., van der Walt, S. J., et al. 2020, *Nature*, 585, 357–362  
 He, K., Zhang, X., Ren, S., & Sun, J. 2015, *Deep Residual Learning for Image Recognition*  
 Holloway, P., Marshall, P. J., Verma, A., et al. 2024, *MNRAS*, 530, 1297  
 Holwerda, B. W., Baldry, I. K., Alpaslan, M., et al. 2015, *MNRAS*, 449, 4277  
 Hsieh, B. C. & Yee, H. K. C. 2014, *ApJ*, 792, 102  
 Huang, X., Storfer, C., Gu, A., et al. 2021, *ApJ*, 909, 27  
 Huang, X., Storfer, C., Ravi, V., et al. 2020, *ApJ*, 894, 78  
 Hunter, J. D. 2007, *Computing in Science & Engineering*, 9, 90  
 Inami, H., Bacon, R., Brinchmann, J., et al. 2017, *A&A*, 608, A2  
 Ivezić, Z., Axelrod, T., Brandt, W. N., et al. 2008, *Serbian Astronomical Journal*, 176, 1  
 Ivezić, Ž., Kahn, S. M., Tyson, J. A., et al. 2019, *ApJ*, 873, 111  
 Jacobs, C., Collett, T., Glazebrook, K., et al. 2019, *ApJS*, 243, 17  
 Jacobs, C., Glazebrook, K., Collett, T., More, A., & McCarthy, C. 2017, *MNRAS*, 471, 167  
 Jaelani, A. T., More, A., Sonnenfeld, A., et al. 2020, *MNRAS*, 494, 3156  
 Jaelani, A. T., More, A., Wong, K. C., et al. 2024, *MNRAS*, 535, 1625  
 Kelly, P. L., Rodney, S., Treu, T., et al. 2023, *Science*, 380, abh1322  
 Lange, S. C., Amvrosiadis, A., Nightingale, J. W., et al. 2024, arXiv e-prints, arXiv:2410.12987  
 Lanusse, F., Ma, Q., Li, N., et al. 2018, *MNRAS*, 473, 3895  
 Laureijs, R., Amiaux, J., Arduini, S., et al. 2011, arXiv e-prints, arXiv:1110.3193  
 Li, R., Napolitano, N. R., Spiniello, C., et al. 2021, *ApJ*, 923, 16  
 Li, R., Napolitano, N. R., Tortora, C., et al. 2020, *ApJ*, 899, 30  
 Li, R., Shu, Y., Su, J., et al. 2019, *MNRAS*, 482, 313  
 Meštrić, U., Vanzella, E., Zanello, A., et al. 2022, *MNRAS*, 516, 3532  
 Millon, M., Courbin, F., Bonvin, V., et al. 2020, *A&A*, 640, A105  
 More, A., Verma, A., Marshall, P. J., et al. 2016, *MNRAS*, 455, 1191  
 Morishita, T., Stiavelli, M., Grillo, C., et al. 2024, *ApJ*, 971, 43  
 Nagam, B. C., Acevedo Barroso, J. A., Wilde, J., et al. 2025, arXiv e-prints, arXiv:2502.09802  
 Paraficz, D., Courbin, F., Tramacere, A., et al. 2016, *A&A*, 592, A75  
 Pascale, M., Frye, B. L., Pielke, J. D. R., et al. 2025, *ApJ*, 979, 13  
 Petrillo, C. E., Tortora, C., Vernardos, G., et al. 2019, *MNRAS*, 484, 3879  
 Planck Collaboration, Aghanim, N., Akrami, Y., et al. 2020, *A&A*, 641, A6  
 Price-Whelan, A. M., Sipőcz, B. M., Günther, H. M., et al. 2018, *AJ*, 156, 123  
 Refsdal, S. 1964, *MNRAS*, 128, 307  
 Rojas, K., Collett, T. E., Ballard, D., et al. 2023, *MNRAS*, 523, 4413  
 Rojas, K., Savary, E., Clément, B., et al. 2022, *A&A*, 668, A73  
 Savary, E., Rojas, K., Maus, M., et al. 2022, *A&A*, 666, A1  
 Schuldt, S., Cañameras, R., Andika, I. T., et al. 2025, *A&A*, 693, A291  
 Schuldt, S., Cañameras, R., Shu, Y., et al. 2023a, *A&A*, 671, A147  
 Schuldt, S., Chirivì, G., Suyu, S. H., et al. 2019, *A&A*, 631, A40  
 Schuldt, S., Suyu, S. H., Cañameras, R., et al. 2023b, *A&A*, 673, A33  
 Schuldt, S., Suyu, S. H., Cañameras, R., et al. 2021, *A&A*, 651, A55  
 Shajib, A. J., Treu, T., Birrer, S., & Sonnenfeld, A. 2021, *MNRAS*, 503, 2380  
 Shajib, A. J., Wong, K. C., Birrer, S., et al. 2022, *A&A*, 667, A123  
 Shu, Y., Bolton, A. S., Kochanek, C. S., et al. 2016, *ApJ*, 824, 86  
 Shu, Y., Brownstein, J. R., Bolton, A. S., et al. 2017, *ApJ*, 851, 48  
 Shu, Y., Cañameras, R., Schuldt, S., et al. 2022, *A&A*, 662, A4  
 Shu, Y., Marques-Chaves, R., Evans, N. W., & Pérez-Fournon, I. 2018, *MNRAS*, 481, L136  
 Sonnenfeld, A., Chan, J. H. H., Shu, Y., et al. 2018, *PASJ*, 70, S29  
 Sonnenfeld, A., Verma, A., More, A., et al. 2020, *A&A*, 642, A148  
 Spergel, D., Gehrels, N., Baltay, C., et al. 2015, arXiv e-prints, arXiv:1503.03757  
 Stein, G., Blaum, J., Harrington, P., Medan, T., & Lukić, Z. 2022, *ApJ*, 932, 107  
 Stiavelli, M., Morishita, T., Chiaberge, M., et al. 2023, *ApJ*, 957, L18  
 Storfer, C., Huang, X., Gu, A., et al. 2024, *ApJS*, 274, 16  
 Suyu, S. H. & Halkola, A. 2010, *A&A*, 524, A94  
 Suyu, S. H., Hensel, S. W., McKean, J. P., et al. 2012a, *ApJ*, 750, 10  
 Suyu, S. H., Huber, S., Cañameras, R., et al. 2020, *A&A*, 644, A162  
 Suyu, S. H., Treu, T., Blandford, R. D., et al. 2012b, arXiv e-prints, arXiv:1202.4459  
 Talbot, M. S., Brownstein, J. R., Dawson, K. S., Kneib, J.-P., & Bautista, J. 2021, *MNRAS*, 502, 4617  
 Tanaka, M., Coupon, J., Hsieh, B.-C., et al. 2018, *PASJ*, 70, S9  
 van der Walt, S., Colbert, S. C., & Varoquaux, G. 2011, *Computing in Science Engineering*, 13, 22

- Van Rossum, G. & Drake, F. L. 2009, Python 3 Reference Manual (Scotts Valley, CA: CreateSpace)
- Vanzella, E., Caminha, G. B., Rosati, P., et al. 2021, *A&A*, 646, A57
- Virtanen, P., Gommers, R., Oliphant, T. E., et al. 2020, *Nature Methods*, 17, 261
- Wang, H., Cañameras, R., Caminha, G. B., et al. 2022, *A&A*, 668, A162
- Wong, K. C., Chan, J. H. H., Chao, D. C. Y., et al. 2022, *PASJ*, 74, 1209
- Wong, K. C., Sonnenfeld, A., Chan, J. H. H., et al. 2018, *ApJ*, 867, 107
- Wong, K. C., Suyu, S. H., Chen, G. C. F., et al. 2020, *MNRAS*
- Zhong, F., Li, R., & Napolitano, N. R. 2022, *Research in Astronomy and Astrophysics*, 22, 065014

## **Appendix A: Color-composite images of re-discovered lens candidates**

In this section we present the color-composite image stamps of the lens candidates that obtained an average grade above 1.5 (i.e. grade A or B) during our visual inspection, but are already known in the literature. We note that the lens candidates discovered by C21, S22, and S25, which we excluded before visual inspection to lower the amount, are not shown.

## **Appendix B: Color-composite images of lens candidates with their predicted mass model**

In this section, we show the color-composite image stamps of the lens candidates in analogy to Figs. 6 and 7, as well as those in Sect. A. Contrary to previous figures, we show here the lens center and Einstein radius for each system predicted by the ResNet of Schuldt et al. (2023a). These models were also shown in one panel during the visual inspection to help the grader classify.

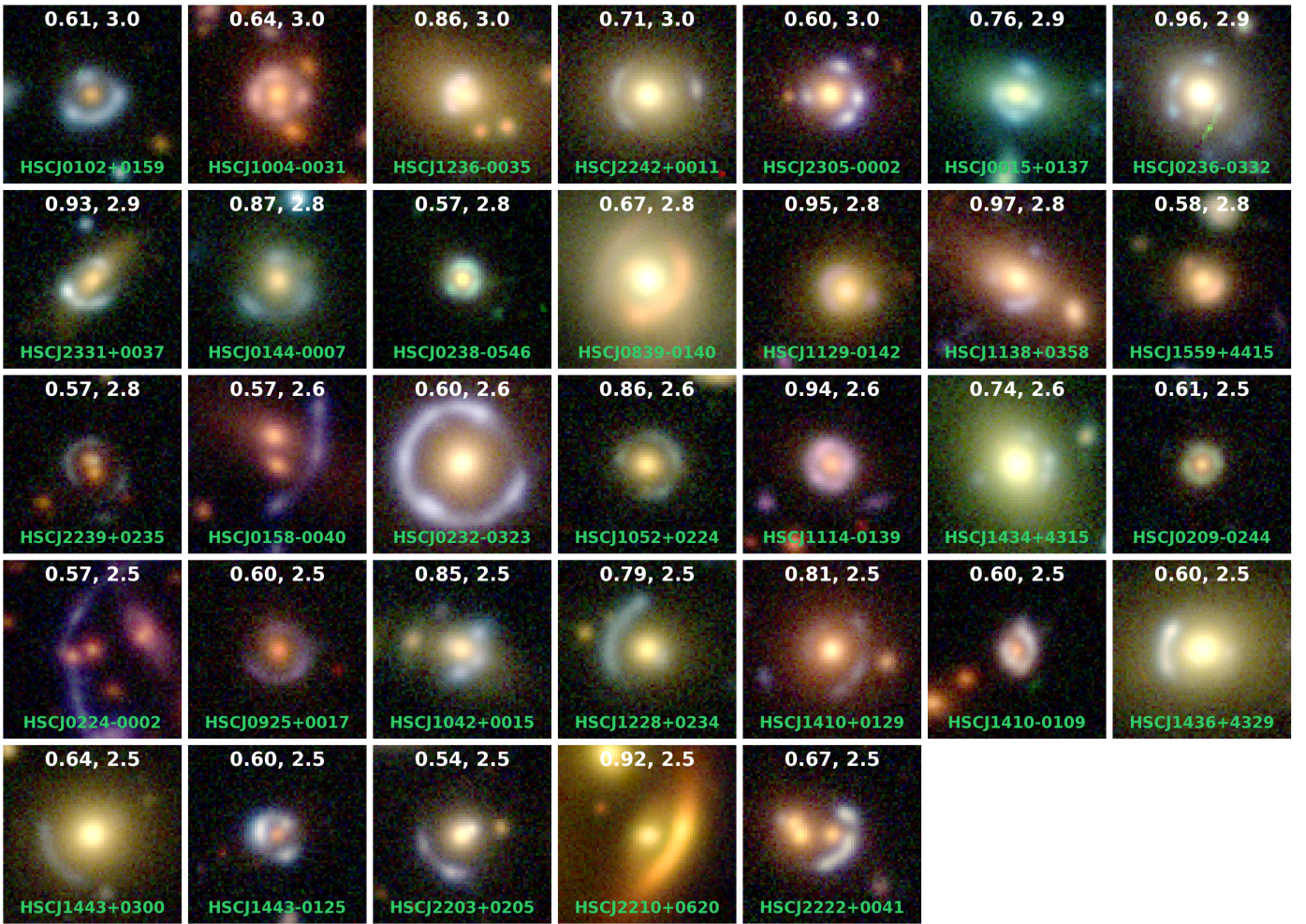


Fig. A.1: Color-image stamps of re-discovered but again visually inspected grade-A lens candidates. Same format as Fig. 6.



Fig. A.2: Color-image stamps of re-discovered but again visually inspected grade-B lens candidates. Same format as Fig. 6.

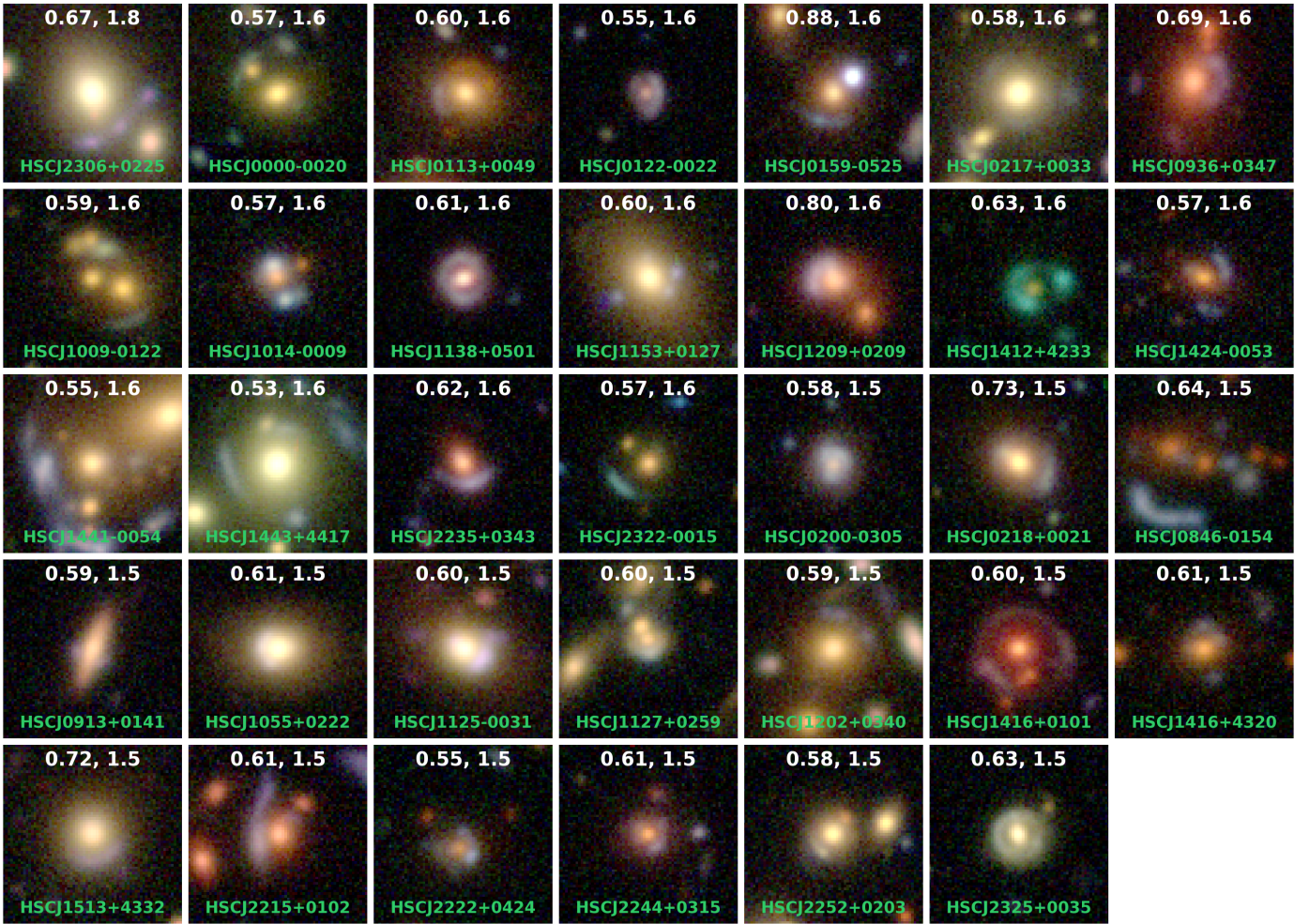


Fig. A.2 (continued): Color-image stamps of re-discovered but again visually inspected grade-B lens candidates. Same format as Fig. 6.

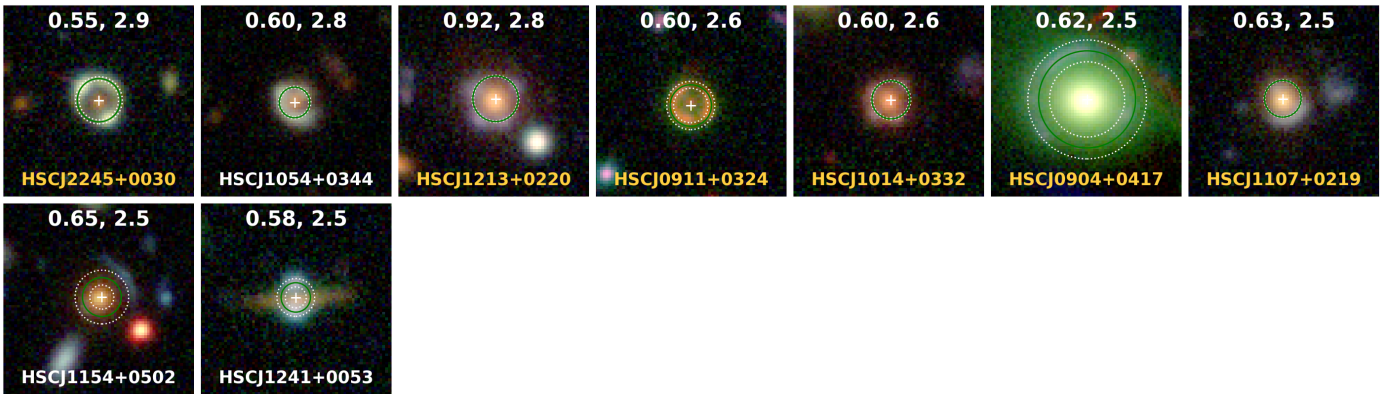


Fig. B.1: Color-image stamps of newly discovered grade A lenses, but showing the lens center and the Einstein radius as green circles predicted by the ResNet of Schuldt et al. (2023a). The predicted  $1\text{-}\sigma$  uncertainty for the Einstein radii are shown with white circles. We mark those with a well predicted lens center and Einstein radius (see also column 30 of Table 2) by yellow names instead of white. Remaining format as Fig. 6.

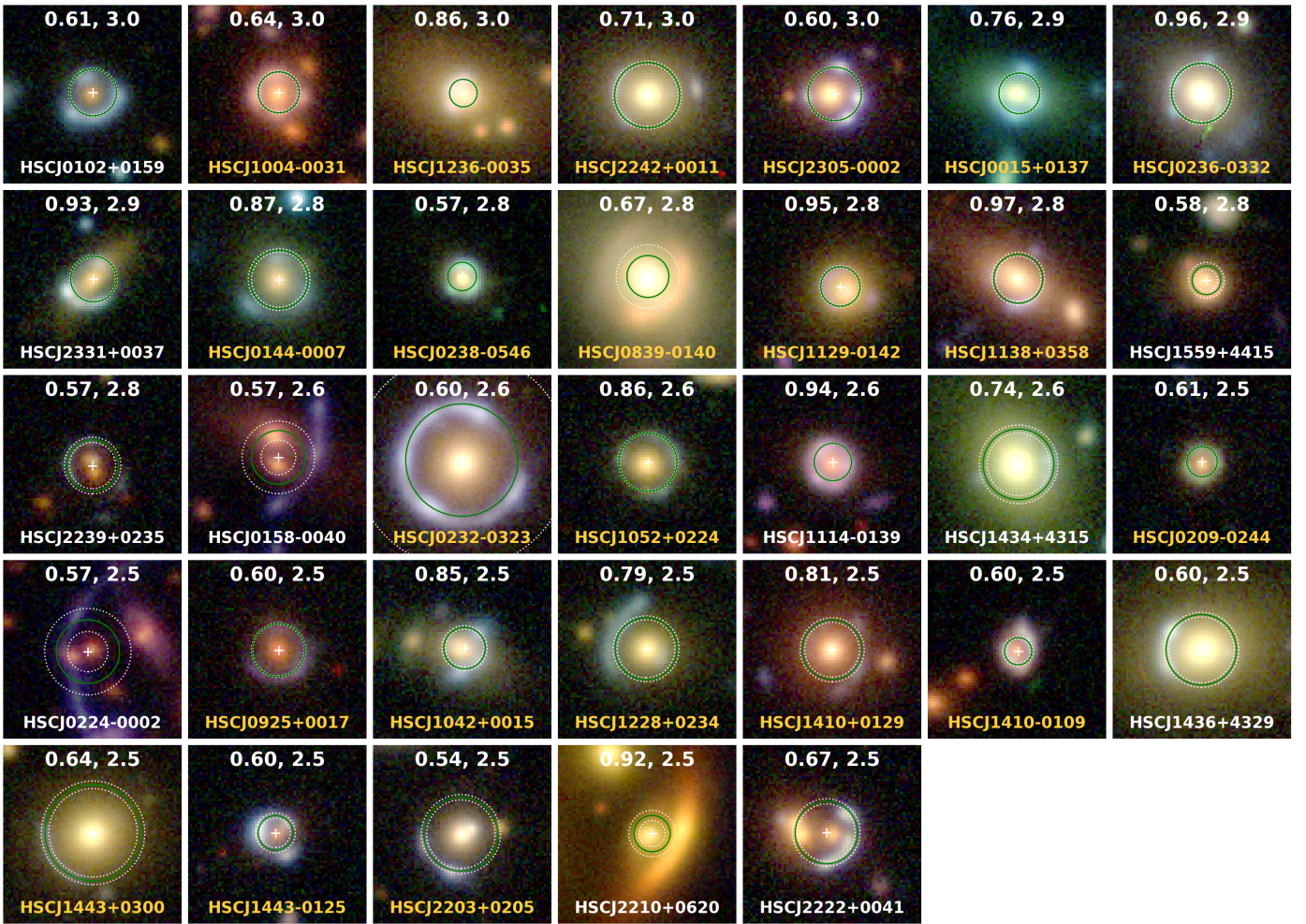


Fig. B.2: Color-image stamps of re-discovered but visually re-inspected grade-A lens candidates. Same format as Fig. B.1.

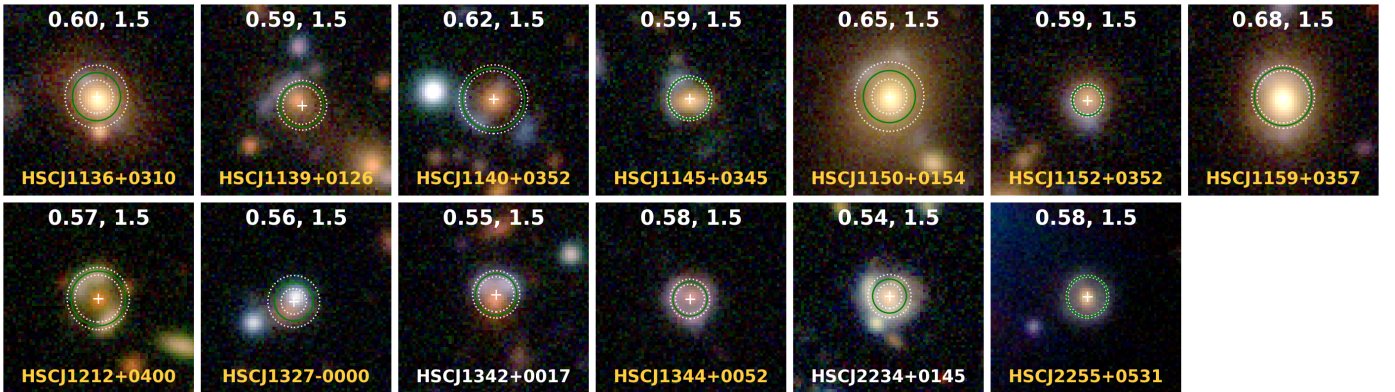


Fig. B.3: Color-image stamps of newly discovered grade-B lens candidates. Same format as Fig. B.1.



Fig. B.3 (continued): Color-image stamps of newly discovered grade-B lens candidates. Same format as Fig. B.1.





Fig. B.4: Color-image stamps of re-discovered but visually re-inspected grade-B lens candidates. Same format as Fig. B.1.

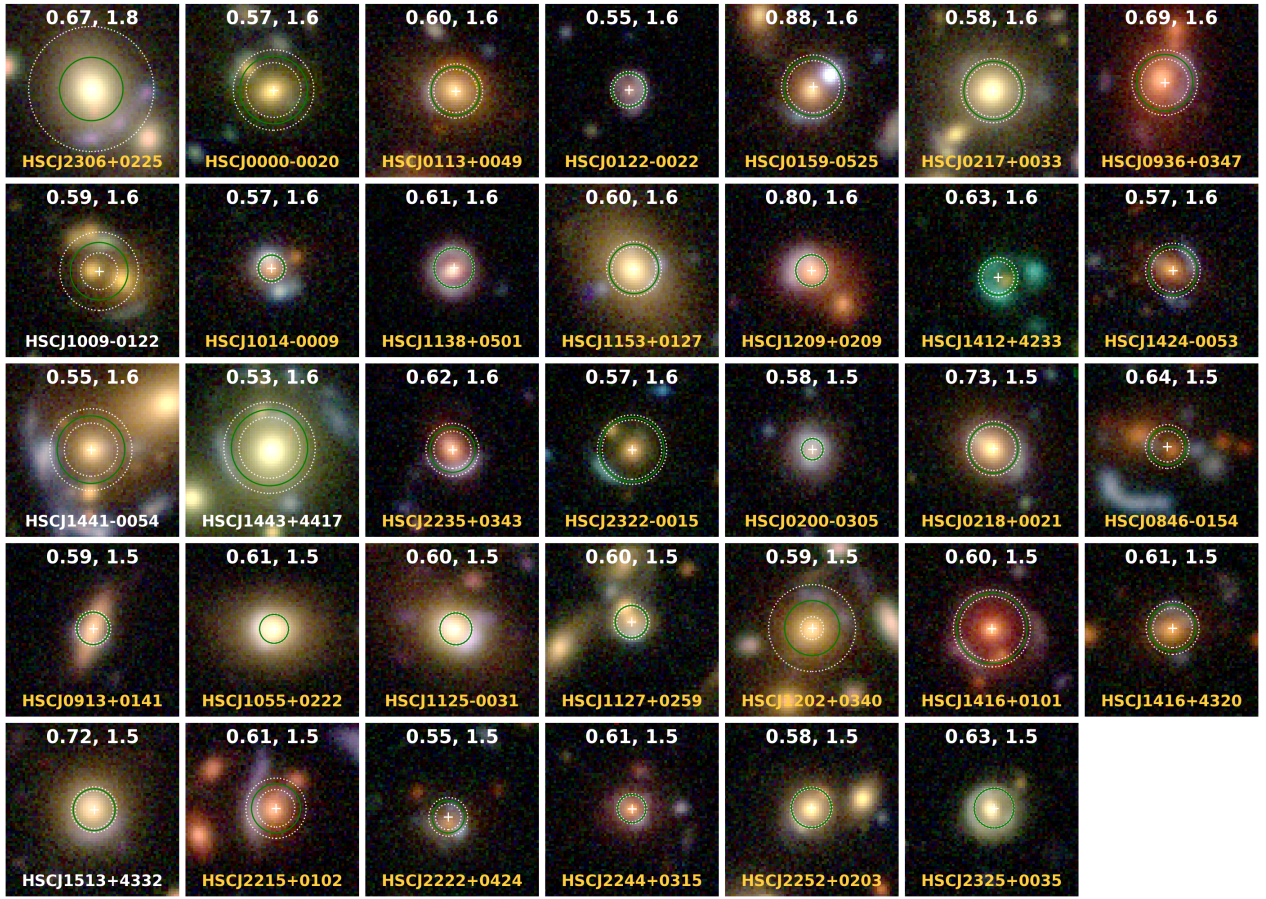


Fig. B.4 (continued): Color-image stamps of re-discovered but visually re-inspected grade-B lens candidates. Format as Fig. B.1.